Journal of Materials Chemistry B

ROYAL SOCIETY OF CHEMISTRY

PAPER

View Article Online
View Journal | View Issue

Cite this: J. Mater. Chem. B, 2024, 12, 9575

Highly disordered and resorbable lithiated nanoparticles with osteogenic and angiogenic properties†

Sara Romanazzo,[ab] Yi Zhu,[c] Rakib Sheikh,[a] Xiaoting Lin,[d] Hongwei Liu,[d] Tong-Chuan He[c] and Iman Roohani *[e]

Received 7th May 2024,
Accepted 9th August 2024

DOI: 10.1039/d4tb00978a

rsc.li/materials-b

In this study, we have developed unique bioresorbable lithiated nanoparticles (LiCP, d_{50} = 20 nm), demonstrating a versatile material for bone repair and regeneration applications. The LiCPs are biocompatible even at the highest concentration tested (1000 μg mL^{-1}) where bone marrow derived mesenchymal stem cells (BM-MSCs) maintained over 90% viability compared to the control. Notably, LiCP significantly enhanced the expression of osteogenic and angiogenic markers *in vitro*; collagen I, Runx2, angiogenin, and EGF increased by 8-fold, 8-fold, 9-fold, and 7.5-fold, respectively. Additionally, LiCP facilitated a marked improvement in tubulogenesis in endothelial cells across all tested concentrations. Remarkably, in an ectopic mouse model, LiCP induced mature bone formation, outperforming both the control group and non-lithiated nanoparticles. These findings establish lithiated nanoparticles as a highly promising material for advancing bone repair and regeneration therapies, offering dual benefits in osteogenesis and angiogenesis. The results lay the groundwork for future studies and potential clinical applications, where precise modulation of lithium release could tailor therapeutic outcomes to meet specific patient needs in bone and vascular tissue engineering.

1. Introduction

Bone fractures and defects are leading causes of global mortality and disability, prompting the development of therapeutic strategies and mechanisms to enhance the bone healing process.[1] A range of natural and synthetic bone substitutes have been developed to enhance the rate and quality of the bone healing process and regeneration.[2–4] One of the most effective strategies is introducing metal ions into such synthetic materials which, upon release, improve biological responses such as bone formation and angiogenesis. This is inspired by the fact that metallic elements exist in extracellular matrices of tissues and play a vital role in maintaining cellular structure, catalyzing biochemical reactions, and facilitating intracellular and extracellular signaling.[5] Within a wide range of metallic elements utilized as bioactive components in bone substitutes, alkali metals are less explored. Alkali metals, characterized by having a single electron in their outermost s-orbital, exhibit similar properties across the group, including low first ionization energies due to their low effective nuclear charges. This single electron facilitates easy ionization, typically forming monovalent ions as these metals achieve noble gas configurations by shedding their outermost electron. Lithium (Li), the lightest and least reactive among them, possesses a small ionic radius and forms a Li^+ cation by losing its valence electron. Despite lithium's lower reactivity and higher solubility, it has a facile transport mechanism into cells and cell organelles *via* several transmembrane processes such as voltage-gated and epithelial Na^+ channels, sodium–lithium counter-transport, sodium–proton pump, and sodium–calcium/lithium exchange on the mitochondrial membrane.[6] Lithium is a known immune regulator[7–9] with osteogenic,[10–20] angiogenic,[21–24] and chondrogenic properties[20,25–27] by promoting several intracellular signaling pathways.[20,28] Recently lithium has been utilized as the main element in the compound,[29] or incorporated into a range of biomaterials including bioactive glasses,[19,24,27,30] calcium silicates,[25,31,32] hydroxyapatite,[33,34] silicon,[35] hydrogels,[36,37] cements[38] and nanofibrous membranes.[39] However, constraints in material formulation and control over release kinetics particularly at a lower dosage, limit the contribution that lithium can

[a] School of Chemistry, Australian Centre for Nanomedicine, University of New South Wales, Sydney NSW, Australia
[b] Australian Centre for NanoMedicine, University of New South Wales Sydney, NSW 2052, Australia
[c] Molecular Oncology Laboratory, Department of Orthopaedic Surgery and Rehabilitation Medicine, The University of Chicago Medical Center, Chicago, IL 60637, USA
[d] Australian Centre for Microscopy and Microanalysis, The University of Sydney, City Road, Sydney, NSW 2006, Australia
[e] School of Biomedical Engineering, University of Technology Sydney, Sydney NSW, Australia. E-mail: iman.roohani@uts.edu.au

† Electronic supplementary information (ESI) available. See DOI: https://doi.org/10.1039/d4tb00978a

bring to the regenerative efficacy of these approaches.[40,41] The dosage is particularly important, as high local concentrations of lithium can adversely influence immune cells to release inflammatory mediators.[42–46] Furthermore, selecting an appropriate host material composition and form (*e.g.*, bulk, nanoparticle, fiber *etc.*) that enable low dosage, sustainable release, and versatility of utilization in tissue engineering strategies has been challenging.[7,34–37,47–51] In this study, we developed for the first time lithiated nanoparticles by incorporating lithium into a structure of amorphous calcium phosphate as a known osteoconductive material with a close composition to the inorganic part of the bone. These nanoparticles are packed with lithium, making them highly versatile for use in various tissue engineering applications. Remarkably, these particles are resorbable and can be utilized in injectable hydrogels, within polymeric meshes, or as coating materials. Furthermore, they are capable of releasing lithium ions at a low dosage, which exhibit potent osteogenic and angiogenic properties *in vitro*, and enable the formation of mature ectopic bone *in vivo*.

Iman Roohani

Dr Roohani is an Associate Professor at the School of Biomedical Engineering, University of Technology Sydney (UTS), and an Adjunct Associate Professor in the School of Biomedical Engineering at the University of Sydney (USyd). His research focuses on the intersection of biology and materials science to explore fundamental biological questions and develop innovative biomaterials for a range of biomedical applications, including translational medicine. His work investigates how cells interact with surfaces and biological entities, particularly their responses to topographical and biochemical signals on various substrates. Dr Roohani's research is also directed towards translational programmes aimed at pioneering novel tissue engineering and 3D bioprinting strategies to regenerate damaged and diseased musculoskeletal tissues. He has led advancements in bioceramics, polymeric biomaterials, and 3D printing technologies. Dr Roohani is the recipient of two prestigious fellowships: the National Health and Medical Research Council Early Career Fellowship and the Sydney Musculoskeletal Health Fellowship. He has authored 75 publications, with an h-index of 34 and over 3 500 citations. He is also the inventor of a single-stage biofabrication technique, COBICS, which creates a 3D heterogeneous bone-analogous microenvironment, and a bioceramic composition licensed by Allegra Orthopaedics. His work has secured over $2 million in funding and has led to translational outcomes, inventions, and numerous accolades, including being a finalist for the Eureka Prize for Innovative Use of Technology in 2023 and the Young Investigator Award of the Year in 2021 (TERMIS).

2. Materials and methods

2.1. Synthesis and characterization of lithiated nanoparticles

All chemicals were purchased from Sigma-Aldrich. Lithium chloride (LiCl, ≥99.98% trace metals basis); calcium nitrate tetrahydrate ($Ca(NO_3)_2{\cdot}4H_2O$, ≥99.0%); sodium phosphate dibasic (Na_2HPO_4, ≥99.0%); ammonium hydroxide solution (NH_4OH, 28% NH_3 in H_2O, ≥99.99%), and ethylene glycol ($C_2H_6O_2$, anhydrous >99.8%). A stock solution containing calcium ions was prepared by dissolving 2.383 g of the calcium nitrate tetrahydrate in ethylene glycol, achieving a final concentration of 0.2 M. A stock solution containing phosphate ions was prepared by dissolving 0.9494 g sodium phosphate dibasic in Milli-Q (MQ) water achieving a final concentration of 0.132 M. A stock solution containing lithium ions was prepared by dissolving 0.42 g of the lithium chloride in ethylene glycol, achieving a final concentration of 0.2 M. Ammonium hydroxide was utilized to adjust the pH of the reaction mixture to 7.45. The LiCPs were synthesized by maintaining the molar ratio of calcium to phosphorus at 1.5, ensuring an optimal stoichiometry conducive to the desired phase composition. The pH of the reaction medium was precisely adjusted to 7.45, to maintain a stable reaction environment conducive to controlled nucleation and growth of the product. Lithium doping was achieved by the gradual addition of lithium to the reaction mixture, targeting a nominal range of lithium atomic ratios from 0.5% to 80%. This approach allowed for the systematic exploration of the effects of lithium concentration on the properties of the final product. The entire reaction mixture was subjected to continuous and vigorous stirring to achieve a homogenous solution, thereby facilitating uniform doping and preventing local supersaturation that could lead to heterogeneous nucleation. As the reaction progressed, solid particles began to precipitate within 4 h. This slow precipitation process is indicative of a controlled reaction environment, allowing for the gradual formation of well-defined solid phases. Upon completion of the precipitation, the solid precipitates were collected through centrifugation, washed three times with Milli-Q water, and dried using a freeze-dryer. The doped concentration of Li was quantitatively measured using a PerkinElmer Nexion 350× inductively coupled plasma mass spectrometer (ICP-MS). The particles were dissolved in 1% HNO_3 and then diluted at a ratio of 1 : 100 before analysis. The particles were chemically characterized with an X-ray diffraction (XRD) technique using a Philips XPERT MPD diffractometer (Cu Kα radiation: λ = 0.154056 nm at 40 kV and 30 mA) over the 2θ range of 20–50° at a scan rate of 0.02° min^{-1}. FT-Raman spectra were recorded on a Bruker MultiRAM spectrometer (Bruker Optics). ACP and doped nanoparticles were dispersed in ethanol using an ultrasonic vibration unit followed by deposition on a copper grid coated with continuing carbon film. The TEM samples were investigated using a field emission transmission electron microscope (FETEM, JEM-2200FS) with the capability of STEM-EDS and Omega-filter for EELS (energy resolution 1.0 eV). Energy filtered bright field images were collected with an objective lens aperture (OLA) inserted and filtered with

zero-loss electrons. Elemental mapping was carried out for the elements Ca ($L_{2,3}$-edge at 346–350 eV) and O (K-edge at 532 eV) using a three-window mapping technique, and P ($L_{2,3}$-edge at 132 eV) and Li (K-edge at 55 eV) using a jump ratio mapping technique. To characterize the release kinetics of lithium from LiCP, the nanoparticles were incorporated into a polycaprolactone (PCL, M_w: 80 000, Sigma-Aldrich) mesh fabricated using the electrospinning technique. To fabricate the meshes, a PCL solution (5% w/v) was prepared by dissolving the polymer in chloroform, followed by the addition of LiCP particles at concentrations of 12 wt%, 6 wt%, and 1.5 wt%. The mixture was then homogenized overnight to ensure uniform distribution of particles. A horizontal electrospinning setup was employed to generate LiCP-containing meshes. A 5 mL solution was loaded into a plastic syringe, which was mounted on a syringe pump set to a flow rate of 0.5 mL h^{-1}. The distance between the needle tip (18 gauge) and the collector, covered with aluminum foil, was set to 25 cm. All meshes were prepared at room temperature with a relative humidity of 45% within a closed chamber and an applied voltage of 15 kV. The produced meshes were cut into square shapes and placed in PBS and MEM-10% FBS. This release study was designed to mimic *in vivo* conditions, where the nanoparticles would be embedded within a matrix rather than freely dispersed. PCL was chosen due to its slow degradation rate and its widespread use as an FDA-approved biomaterial known for its excellent biocompatibility, as well as to demonstrate that LiCP can release lithium within an enclosed, slow-degrading matrix—an important feature for applications where controlled release is essential.

2.2. Cell culture

Human bone marrow derived stem cells (BM-MSC) were purchased from Lonza (catalog number PT-2501 and lot number: 0000654251) and cultured in low-glucose Dulbecco's modified Eagle's medium (DMEM) supplemented with 10% fetal bovine serum (FBS, Bovogen) and 1% penicillin/streptomycin (P/S, Invitrogen). We will hereafter refer to such medium as the proliferation medium. Media were changed twice a week and cells were passaged using a solution containing 0.05% trypsin-EDTA (Thermo Fisher Scientific) when 70% confluence was reached. All experiments were performed with cells at passage between 5 and 9. BM-MSCs at different passages were confirmed to maintain their typical morphology and markers, such as CD105 and Stro-1 (Fig. S1, ESI†). Human dermal microvascular endothelial cells (HMVECs), used for performing tubulogenesis assay, were purchased from Lonza (catalog number CC-2527 and lot number 0000649177). HMVECs were cultured on tissue culture plastic coated with attachment factor (Life Technologies) in endothelial growth media-2 (EGM-2)-supplemented media (Lonza). The endothelial medium was changed every 2 days and the cells were passaged at around 80% confluency. All experiments were performed with HMVECs at passage between 3 and 5. All cell types were cultured at 37 °C, 5% CO_2 in a humidified incubator.

2.2.1. MSC osteogenic differentiation, endothelial differentiation. The osteogenic medium used in the experiments consisted in low glucose DMEM supplemented with 10% FBS, 1% P/S, 100 nM dexamethasone (Sigma-Aldrich, cat. no. D8893-1MG), 50 μM ascorbic Acid (Sigma-Aldrich, cat. no. G9442), and 10 mM β-glycerol phosphate (Sigma-Aldrich, cat. no. BP461). To briefly describe the experimental settings, BM-MSCs were seeded at an initial cell density of 2×10^4 cells per well in a 24 multi-well dish. BM-MSCs were switched to osteogenic medium 24 h after cells adhered onto the tissue culture plates. The osteogenic medium changes were performed every 3 days. Endothelial differentiation of BM-MSCs was induced by using EGM-2 supplemented medium (Lonza, catalog number CC-3202), the same type of medium used for culturing HMVECs. Similarly to cells undergoing osteogenic differentiation, BM-MSCs were seeded at an initial density of 2×10^4 cells per well in a 24 multi-well dish, in standard proliferation medium. Upon overnight incubation, proliferation medium was replaced with the EGM-2 supplemented medium, also called endothelial medium, which was replaced every second day, up to 7 days.

2.2.2. Cytotoxicity assay. For BM-MSCs viability and proliferation studies, cells were seeded in the presence of different concentrations of LiCP at an initial cell density of 2×10^4 cells per well in a 24 multi-well dish. After the cells were cultured for 1 and 7 days, cell viability was analyzed using MTT assay (Sigma Chemical) according to the manufacturer's instructions. Briefly, cell culture medium was removed and replaced with 25 μL of 2.5 mg mL^{-1} MTT solution to each well. After incubation for 2 h at 37 °C, the MTT solution was removed and 100 mL dimethyl sulfoxide (DMSO) was added to each well and mixed for 10 min on a shaker. The absorbance was read at 590 nm in the microplate reader of the Thermo Scientific Multiscan EX (Thermo Fisher Scientific).

2.2.3. Quantitative RT-PCR analysis. For mRNA expression analysis of BM-MSCs cultured either in standard culture medium or in the presence LiCP nanoparticles, cells were maintained in culture for 7 days at 37 °C, in 5% CO_2 and 20% O_2. Subsequently, cells were collected from each sample by 0.25% trypsin-EDTA treatment, and a standard RNA isolation protocol was performed with RNAeasy mini kit according to the manufacturer's instructions (Qiagen). 500 ng of total RNA was reverse-transcribed into cDNA with a random hexamer primer using a high-capacity cDNA reverse transcription kit (Applied Biosystems) according to the manufacturer's instructions and then reverse transcription-polymerase chain reaction (RT-PCR) was performed using a CFX96 real-time detection system (Biorad). The reaction mixture was composed of 10 μL of SYBR Select Master Mix (Applied Biosystems), 10 pmol each of the forward and reverse primers, 2 μL of cDNA, and distilled water to a final volume of 20 μL. The thermocycling conditions were 95 °C for 30 s, followed by 40 cycles of 95 °C for 5 s and 60 °C for 34 s. Normalization of the data was performed using the housekeeping gene glyceraldehyde-3-phosphate dehydrogenase (GAPDH) as an endogenous control in the same reaction as the gene of interest. The primers used in this study are listed in Table S1 (ESI†). The specificity of the SYBR PCR signal was confirmed by melt curve analysis. Ct values were transformed into relative quantification data using the $2^{-\Delta\Delta Ct}$ method, and data were normalized to GAPDH mRNA expression.

2.2.4. Histological and activity quantification analysis. Samples were fixed in 4% paraformaldehyde (Bio-Strategy Ltd) solution for 15 min at room temperature at the desired time point. Total collagen presence was investigated using picrosirius red staining. Picrosirius red solution 0.1% was prepared with Direct Red 80 (Sigma 365548) and saturated aqueous solution of picric acid (Sigma P6744). The qualitative detection of alkaline phosphatase (ALP) was performed by staining the fixed samples with an ALP substrate solution composed of 0.2 mg mL^{-1} Naphtol AS-MX phosphate and 0.4 mg mL^{-1} Fast Red TR (all from Sigma). ALP activity was measured using the ALP diethanolamine activity kit (Sigma) following the manufacturer's instructions.

2.2.5. *In vitro* tubulogenesis assay. An *in vitro* tubulogenesis assay was performed by adding 25 mL of Geltrex LDEV-Free Reduced Growth Factor Basement Membrane Matrix (Thermo Fisher, USA) to coat 48-well plates and then incubated at 37 °C for 30 min, to allow gel formation. Next, 1.5×10^4 HMVECs at passages between 4 and 7 were seeded in each well in 100 μL of unsupplemented EBM-2 medium (Lonza, USA, catalog number: CC-3156, lot number: E0001149364) and 400 μL of conditioned medium, collected from each experimental group, was added to each well. Fully supplemented EGM-2 medium (catalog number: CC-4147) was used as a positive control, whereas unsupplemented EBM-2 medium was used as a negative control. Tube formation was assessed 8 h after cell seeding, by imaging samples by using an Olympus CKX53 microscope at 20× magnification. The tube area was then quantified using the ImageJ plugin ''Angiogenesis analyzer'' (written by Gilles Carpentier, 2012, available at: **https://imagej.nih.gov/ij/macros/toolsets/Angiogenesis%20Analyzer.txt**). Among all parameters measured through the plugin, total master segment length was chosen to compare the different groups. In addition, after tube formation assessment at 8 hours post-seeding, samples were fixed with 4% paraformaldehyde (Bio-Strategy Ltd) for 15 min at room temperature, and subsequently stained to detect cytoskeleton and nuclei as described in the next section ''Immunofluorescence staining''.

2.2.6. Immunofluorescence staining. In order to analyze BM-MSCs' morphology and their expression of osteogenic markers, cells were cultured on cell-culture treated cover slips (Thermo Fisher Scientific) and then fixed with 4% paraformaldehyde (Bio-Strategy Ltd) solution for 15 min at room temperature at the desired time point. Subsequently, cell membranes were permeabilized by incubation in 0.1% Triton X-100 for 30 min. For cell shape analysis, samples were incubated with tetramethylrhodamine-conjugated phalloidin diluted in 1% bovine serum albumin (BSA) (1 : 100; Invitrogen) for 1 h at room temperature. Nuclei were counterstained with DAPI (Invitrogen). Cell area and shape were quantified using ImageJ software. For each image, individual cells were manually traced to delineate cell boundaries. The following parameters were measured: – cell area, calculated as the number of pixels within the traced boundary, converted to square micrometers using the known pixel-to-micron ratio; – cell aspect ratio: defined as the ratio of the major axis to the minor axis of the cell, obtained from the best-fit ellipse of the traced boundary. The two parameters were reported as mean ± standard deviation. For osteogenic markers staining, samples were incubated for 1 h at room temperature in a solution of primary antibody diluted in BSA 1% at a 1 : 200 ratio for collagen type I (Abcam 90395), and then the appropriate secondary antibody anti-mouse 488 (1 : 200) in 1% BSA was used. Samples were then mounted on glass slides and imaged with the Nikon A1 confocal microscope. In order to measure each of the signal intensity, each acquired image was converted into a greyscale image, then the integrated density was measured and normalized to the number of cells. For each group, 5 images were taken randomly within the sample, with $n = 3$.

2.3. *In vivo* study

2.3.1. Ectopic bone formation using a hydrogel scaffold *in vivo*. The Institutional Animal Care and Use Committee (IACUC) approved all animal procedures in this study (ACUP protocol #71108). The animal-related experimental protocols were carried out under the guidelines of IACUC. The subcutaneous ectopic bone formation was performed as previously described.[52–57] To prepare collagen hydrogels, acid solubilized Type 1 collagen from bovine skin (3 mg mL^{-1}, C4243 Sigma Aldrich) was reconstituted in an ice bath to a final concentration of 2 mg mL^{-1} in phosphate-buffered saline. The pH was adjusted to 7.4 by neutralizing the hydrogel precursors with 1 N NaOH. At this point, the nanoparticles were mixed and homogenized before being transferred to the incubator. Designated silicon molds containing cylindrical-shaped cavities with a diameter of 5 mm and a height of 6 mm were filled with the collagen–nanoparticle mixture. The mixture was then incubated in a humidified 5% CO_2 environment at 37 °C for 30 min to facilitate fibrillogenesis. Three groups were set up: (1) collagen hydrogel, (2) collagen hydrogel containing 1 mg mL^{-1} of LiCP and (3) collagen hydrogel containing 1 mg mL^{-1} of ACP. The mouse BM-MSCs were collected and resuspended in 50 μL of collagen hydrogel. The mixture was subcutaneously injected into the flanks of athymic nude mice (n = 5/group, 6–8 weeks old, female; Envigo/Harlan Research Laboratories; 2×10^6 cells per site). Four weeks after the initial injection, all mice were sacrificed for harvesting ectopic masses from the injection sites.

2.3.2. Hematoxylin & eosin (H & E) staining and trichrome staining. After μCT imaging, the retrieved specimens were decalcified for 3 days and subjected to paraffin-embedding. Serial sections at 5 mm of these paraffinized masses were deparaffinized and then subjected to histological staining as reported.[58–60] The average % of trabecular bone area from each sample group was quantitatively assessed by analyzing high power fields using the ImageJ program.

2.4. Statistical analysis

Results are expressed as mean ± standard deviation of the mean of $n \geq 3$ independent experiments. Statistical analyses were performed using GraphPad Prism (version 9) software. One- or two-way analysis of variance (ANOVA) were used for analysis of variance to compare between groups.

3. Results and discussion

Fig. 1a illustrates the relationship between the nominal concentration of lithium in the precursor solution and the amount of lithium doping into amorphous nanoparticles. The data reveal a non-linear relationship, with an increasing trend in the amount of lithium doped as the concentration in the precursor solution rises. However, the efficiency of doping remains relatively low, reaching a plateau that suggests the presence of an energy barrier which likely expels lithium ions from entering the structure of the nanoparticles. XRD profiles of the doped samples show that all peaks are broad, consistent with an amorphous structure, but with an increase in lithium content; these peaks shift slightly to the left and become broader, indicating structural changes within the nanoparticles. While shifts in XRD peaks can be attributed to various factors, including instrumental and physical effects, mechanical stress or strain, and differences in sample form and preparation—such as the introduction of strain or preferred orientation—in this instance, the observed shift correlates with the incremental addition of lithium, with all other variables remaining constant. We attribute this shift to lattice expansion, caused by the progressive interstitial incorporation of Li^+ ions, which accommodates differences in ionic size and charge. Fig. 1b compares the Raman spectra of ACP and LiCP (ACP-0.2 atom% Li), particularly highlighting the significant differences introduced by doping. The Raman spectra of all doped concentrations are presented in Fig. S2 (ESI†). LiCP exhibits distinctive new peaks at 860 cm^{-1}, which can be attributed to the stretching vibrations of O–O bonds in $LiOOH{\cdot}H_2O$,[61] and at 676 cm^{-1} and 732 cm^{-1}, associated with LiOH.[62–64] Both types of nanoparticles show similar phosphate-related bands: the symmetric stretching mode P–O at 950 cm^{-1}, the asymmetric stretching mode of phosphate between 400–440 cm^{-1}, and complex bending and stretching of phosphate between 570–590 cm^{-1}. Notably, ACP exhibits a peak at 1010 cm^{-1}, indicative of the HPO_4 group, a key indicative peak of octacalcium phosphate, which is absent in LiCP. Instead, LiCP displays a unique peak at 992 cm^{-1}, corresponding to HPO_4^{2-}. Another significant difference between LiCP and ACP is that Raman peaks of LiCP are broader and noisier suggesting a higher level of molecular disorder, likely due to the densely packed lithium ions and interacting with calcium and phosphate bonds. ACP is a structurally disordered and hydrated phase with a stoichiometry similar to tricalcium phosphate. This disordered structure provides interstitial sites where

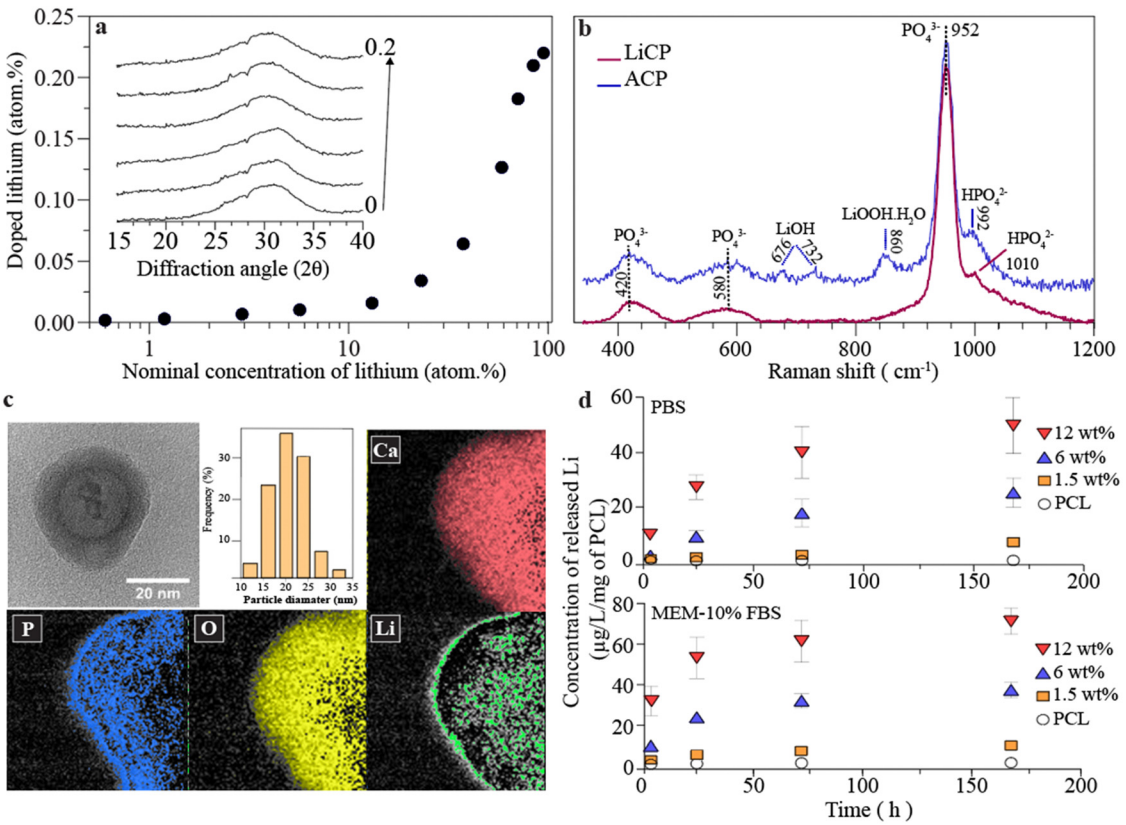

Fig. 1 Lithium doping in amorphous calcium phosphate nanoparticles and their characterisation. (a) Relationship between nominal lithium concentration in the precursor solution and lithium doping efficiency. (b) Raman spectra of ACP and LiCP (ACP-0.2 atom%), highlighting distinct spectral differences due to lithium incorporation. (c) TEM micrograph and elemental mapping of LiCP nanoparticles, showing size distribution and lithium localization. The high-contrast fringe layer visible around LiCP in the element mapping images is due to limitations of the jump ratio method and should not be interpreted as lithium segregation at the surface. Lithium is predominantly localized in the core of the nanoparticles. (d) Release kinetics of lithium ions from LiCP embedded in polycaprolactone meshes in PBS and MEM-10% FBS.

lithium ions can be incorporated, particularly at low concentrations. The appearance of additional peaks and slight shifts in the characteristic phosphate bands observed in the Raman spectra following the incorporation of Li^+ suggest interactions between lithium and the ACP matrix. The peak at $\sim$952 cm^{-1}, attributed to the symmetric stretching mode ($\nu1$) of the PO_4^{3-} group, remains largely unchanged with lithium incorporation, indicating that the primary phosphate structure is preserved. This suggests that lithium does not disrupt the core framework of the phosphate groups. However, shifts in the phosphate stretching modes ($\sim$420 cm^{-1} and $\sim$580 cm^{-1}) imply the formation of stable complexes through interactions between Li^+ and the negatively charged PO_4^{3-} groups. Additionally, the coordination of lithium with hydroxyl groups, as evidenced by the presence of Li–OH and LiOOH bands in the Raman spectra, likely contributes to the hydration and stabilization of the ACP phase. This coordination helps to prevent crystallization, maintaining the disordered structure characteristic of ACP. Therefore, the bonding between lithium and ACP nanoparticles is likely a combination of interactions with phosphate groups and coordination with hydroxyl groups, which collectively contribute to the stabilization of the amorphous structure. Fig. 1c presents a transmission electron microscopy (TEM) micrograph of LiCP nanoparticles, showing a particle size distribution ranging from 10–35 nm with a median size of 20 nm. There is a noticeable difference in the particle size of ACP particles with increasing concentrations of doped lithium, where the size decreases from approximately 60 nm to 20 nm (Fig. S3, ESI†). Elemental mapping confirms the presence of calcium, phosphorus, oxygen, and lithium, with lithium ions predominantly located in the core of the particles. Fig. 1d evaluates the release kinetics of lithium ions from LiCP embedded in polycaprolactone (PCL) meshes submerged in phosphate-buffered saline (PBS) and minimum essential medium supplemented with 10% fetal bovine serum (MEM-10% FBS). The results demonstrate an effective, concentration-dependent release of lithium ions, which is sustained over time in both environments. This sustained release refers to the gradual and continuous release of lithium ions over time, as opposed to an immediate or burst release, indicating the potential of these nanoparticles for controlled therapeutic applications.

To study the biotoxicity of the developed LiCP nanoparticles, BM-MSCs were placed in culture with a range of nanoparticle concentrations (from 1 μg mL^{-1} to 1 mg mL^{-1}), either in direct or indirect culture methods. In the direct culture assays, cells were exposed to LiCP directly within the culture medium (Fig. 2a). On day 1, cell viability across the groups did not show any significant difference. Notably, even at the highest concentration, cells retained over 90% viability relative to the control. By day 7, the trend of decreased viability with increased LiCP concentration became clear. As a result, the cell activity became 1-fold lower than the control group, in the presence of 1000 μg mL^{-1} nanoparticles. The overall metabolic activity of the cells up to 500 μg mL^{-1} LiCP concentrations, appeared to improve when compared to day 1, suggesting some adaptation or recovery from the initial exposure.

For the indirect culture condition, LiCP was introduced into the cell culture medium, prior to its addition to cells in culture plates. The aim of this assay was to assess if any leaching product released from the LiCP could affect cell bioactivity. At day 1 of exposure, there was no significant difference among groups; in contrast to the direct co-culture, cells were able to maintain a metabolic activity comparable to the non treated control even by day 7 (Fig. 2b). Thus, we can conclude that the indirect culture of cells with LiCP did not show any effect on cell viability and proliferation.

Cell morphology has been tightly connected to nanoparticle cellular uptake ability.[65] In order to understand the influence of LiCP into cell shape, BM-MSCs have been exposed at safe concentrations of nanoparticles (up to 250 μg mL^{-1}), in conjunction with either proliferation or osteogenic differentiation medium up to 28 days. Cell morphology of BM-MSCs was assessed by specifically looking at cell aspect ratio and cell area parameters over time. While control cells exhibited a typical elongated shape of mesenchymal stem cells cultured on plastic and under proliferation conditions, cells exposed to a higher concentration of LiCP showed a more rounded phenotype (Fig. 3a), corresponding to a significant decrease in aspect ratio (Fig. 3c). In fact, on day 7, in proliferation medium, the aspect ratio decreased significantly with increased LiCP concentration, indicating that cells become less elongated with higher LiCP levels. The effect was most pronounced at 250 μg mL^{-1}. The same trend was maintained after 28 days, however, the difference became less noticeable, due to the natural tendency of cells to become compact when reaching confluence. The peculiar cuboidal cell shape resembling osteoblast-like cells was particularly observed when BM-MSCs were in the presence of LiCP at a concentration of 100 μg mL^{-1} (Fig. 3a), and this was also confirmed by diminished cell area compared to the control cells (Fig. 3d). When cultured in osteogenic medium, the cells were generally less elongated, corresponding to an overall lower aspect ratio, with significant decrease both at day 7 and 28 for control cells when compared to cells under proliferation conditions. For BM-MSCs exposed to LiCP, the difference became significant only at day 28, showing the 100 μg mL^{-1} group as the one with the most dramatic change in cell shape (Fig. 3b and c). In respect to cell area, there was a reverse correlation to LiCP concentration, both at 7 and 28 days (Fig. 3d). Cell size quantification also revealed a size reduction of cells in the presence of osteogenic medium compared to control cells under proliferation conditions. The cell area undergoing osteogenic differentiation further diminished after 28 days, compared to at 7 days (Fig. 3d).

Overall, the results suggest that LiCPs affect cell morphology, with higher concentrations leading to less elongation (lower aspect ratio) and a smaller cell area. These effects are also dependent on the medium and are more pronounced at the earlier time point (day 7) than at day 28. The significant decrease in aspect ratio at higher concentrations may suggest that LiCP affects cytoskeletal organization or that there is a shift in the cell status. Interestingly, the only addition of the nanoparticles, without chemical contribution of supplemented

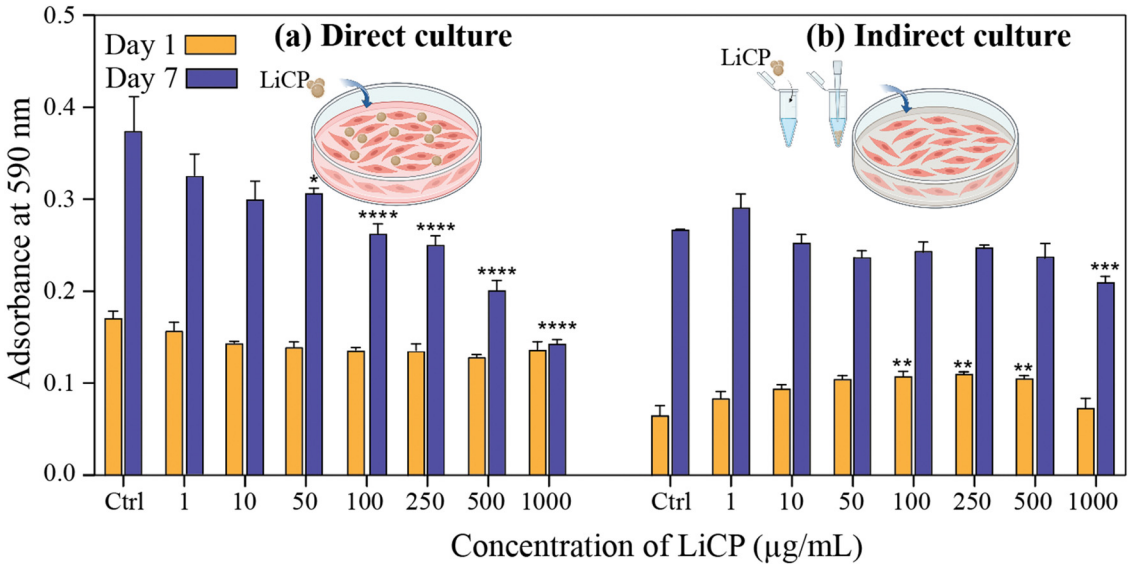

Fig. 2 BM-MSCs survival rate in presence of LiCP. Cell viability and proliferation was calculated by MTT assay, in direct (a) and non direct (b) culture with increasing concentrations of LiCP, after 1 and 7 days of exposure. Control groups (Ctrl) consisted of cells cultured in the absence of nanoparticles. Statistical analysis was performed by comparing each group to the control group at each time point. *$p < 0.02$, ** $p < 0.01$, *** $p < 0.001$, **** $p < 0.0001$.

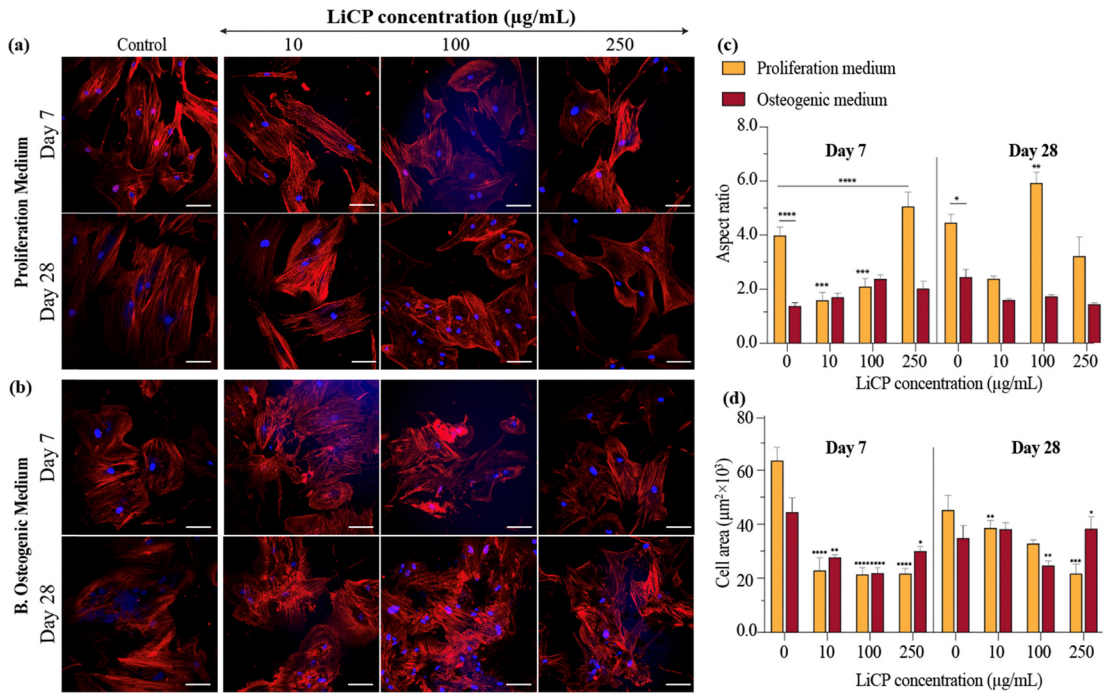

Fig. 3 Representative images of BM-MSCs cultured in the presence of LiCP (10 100 or 250 µg mL^{-1}), either in proliferation (a) or osteogenic medium (b) for up to 28 days. Cell shape (c) and cell size (d) quantification. Scale bars: 100 µm. Statistical analysis was performed by comparing each group to the control group at each time point. *$p < 0.02$, ** $p < 0.01$, *** $p < 0.001$, **** $p < 0.0001$.

osteogenic medium, was enough to significantly reduce the cell area at all LiCP concentrations after 7 days of culture. After 28 days, the parameter returned mostly comparable to control, highly suggesting the cellular uptake of nanoparticles in the first days and subsequent degradation. Moreover, the changes in aspect ratio and cell area from day 7 to day 28 indicate that cells respond to LiCP not only based on concentration but also over time. Cells might initially respond to the presence of LiCP by altering their shape, but with prolonged exposure, they could potentially activate compensatory mechanisms that modify

their morphology differently. The addition of osteogenic medium, showing generally lower aspect ratio, suggests a change in cell morphology due to their choice in differentiating to osteoblasts, which are typically less elongated cells compared to mesenchymal stem cells. Potential signaling pathways that could be involved in cell shape change as a first step, include the Wnt signaling pathway, which is known to be affected by lithium ions and is critical for both cell proliferation and osteogenesis.[66,67]

Having proved an effect on cell morphology, to identify LiCP influence on BM-MSC osteogenic differentiation, these cells were cultured in the presence of LiCP at three different concentrations, 10, 100 or 250 μg mL^{-1}, and evaluated for their ability to deposit collagen type I, which is the main organic component of bone's extracellular matrix (ECM). Picrosirius Red stains at day 21 showed larger total collagen deposition in samples in culture with 250 μg mL^{-1} LiCP in proliferation medium, however, the upregulation was not significant compared to the control (Fig. S4, ESI†). Collagen type I detection at day 28 showed significant differences between groups (Fig. 4). As LiCP concentration in the media increased, there was a notable increase in collagen deposition, particularly at 10 μg mL^{-1}, with an 8-fold change compared to the non-treated control. At 100 and 250 μg mL^{-1}, the staining appeared less intense than at 10 μg mL^{-1} but was still higher than the control (Fig. 4a and b), with 250 μg mL^{-1} statistically higher than the control. The increase in collagen I became linear with nanoparticle concentration when the cells were switched to osteogenic medium, suggesting a synergistic effect of biochemical and physical components (Fig. 4c). Cells in proliferation medium showed sensitivity to LiCP with enhanced osteogenic potential compared to the control, when nanoparticles were at the lower end (Fig. 4b). The reduced fold-change at high concentrations could be due to an inhibitory activity. However, the fact that when LiCP were combined with osteogenic medium, the cells were able to express higher collagen I (Fig. 4c), suggests a potential ability of the nanoparticles to help deliver the chemical components of the medium inside the cells. Cells in osteogenic medium also appeared to proliferate to a greater extent compared to the ones in proliferation medium. These results suggest a mature differentiation of the cells when exposed to LiCP in combination with chemical osteogenic induction.

Gene expression of the early osteogenic differentiation marker Runx2 was significantly upregulated in all groups treated both with LiCP and osteogenic supplements (Fig. 5a, left). When in presence of proliferation conditions, Runx2 was significantly upregulated only at the highest concentration of nanoparticles. Similarly, osteocalcin, another marker indicative of osteoblast phenotype, directly increased with LiCP concentration, with the highest expression when samples were co-treated with nanoparticles and osteogenic chemical supplements (Fig. 5a, center). Interestingly, collagen I gene expression was downregulated in all groups compared to the control. Collagen I is a major component of the bone matrix. The trend is somewhat different from the other two markers, showing decreased expression compared to the control, in the presence of PM, and slightly higher but not significant expression when in combination with OM (Fig. 5a, right). The variability in these markers' expression might be attributed to the sequential order in which they manifest throughout the osteogenic differentiation process, with collagen I typically being one of the last elements to emerge.

The genetic expression of endothelial markers, associated with endothelial functions and angiogenesis, varied across the three markers analyzed. EGF, involved in the proliferation of endothelial cells marked peak at 250 μg mL^{-1} LiCP concentration in osteogenic medium (OM) (Fig. 5b, left). VEGF, critical for the growth of new blood vessels, was increased only in the 100 μg mL^{-1} LiCP group and significantly decreased in all nanoparticle samples when in OM (Fig. 5b, center). In contrast, angiogenin, another factor involved in angiogenesis, was upregulated in all groups treated with nanoparticles, with the highest fold changed expression in 100 μg mL^{-1} LiCP, both in growth and osteogenic medium (Fig. 5b, right). The interplay between angiogenesis and osteogenesis is known to be vital

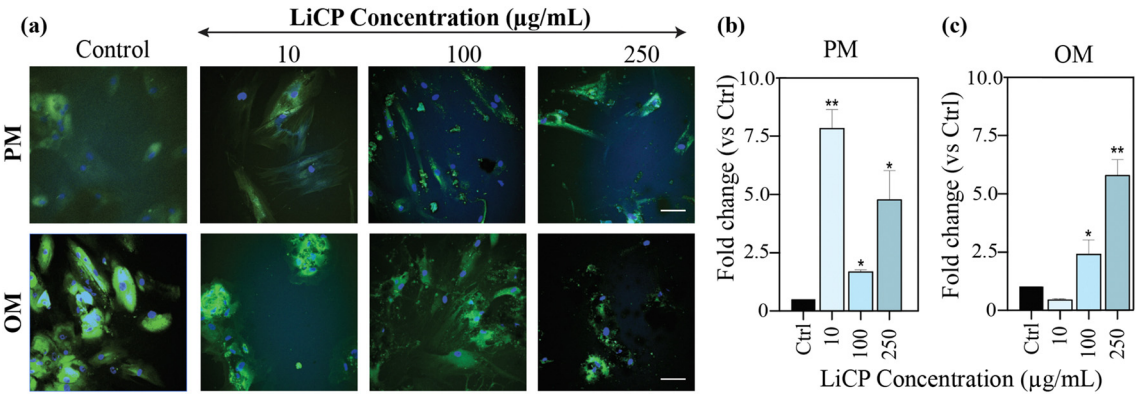

Fig. 4 Representative immunohistochemical images of collagen type I in BM-MSCs cultured in the direct presence of LiCP, in combination with proliferation (a, top) or osteogenic (a, bottom) medium for 28 days; collagen I expression is shown in green and nuclei were counterstained in blue (DAPI). Scale bars: 100 μm; relative fluorescence intensity quantification compared to the control (Ctrl) in proliferation (PM) (b) or osteogenic (OM) (c) medium. ** $p < 0.01$, *$p < 0.02$.

during the process of intramembranous ossification. VEGF operates within a delicate balance to maintain bone homeostasis and optimal physiological levels. Insufficient VEGF can disrupt osteoblast differentiation, whereas an excess can heighten osteoclast recruitment, which in turn, could lead to bone resorption. In the context of bone repair, osteoblasts generate VEGF, encouraging endothelial cell migration and proliferation. These endothelial cells, once activated, contribute to the osteogenic process by releasing factors such as bone morphogenetic protein (BMP)-2 and BMP-4, fostering further osteoblast differentiation.

The osteogenic differentiation of BM-MSCs under the different culture conditions was confirmed, by qualitative and quantitative assessment of ALP activity levels, an early marker of differentiation, along the time of culture. ALP activity was confirmed in all experimental groups apart from the negative control consisting of cells in proliferation medium under standard culture conditions, with and without chemically conditioned osteogenic medium (Fig. 6a). ALP quantitative analysis also confirmed augmented ALP production in groups containing LiCP under proliferation conditions, compared to the control. When comparing samples at day 14 with the ones at day 28, we could notice an overall increase in the ALP activity, as expected (Fig. 6c and Fig. S5, ESI†). Cells cultured in all three concentrations of LiCP positively expressed ALP in a similar intensity in proliferation conditions, whereas when osteogenic medium was added to the culture, a clear increase of ALP staining was evident (Fig. 6a). Quantitative analysis confirmed increasing ALP activity when cells were exposed at both LiCP and osteogenic medium (Fig. 6c), as noticed in the staining as well (Fig. 6a, right). The ALP activity was significantly enhanced by increasing the concentrations of LiCP in OM (Fig. 6c).

As BM-MSCs are multipotent adult stem cells, they are able to differentiate into multiple cell types.[68] There has been evidence of trans-differentiation of MSCs into endothelial cells, obtained by a variety of methods, such as usage of pre-differentiation medium before transferring cells into Matrigel culture,[69] flow chamber systems,[70] co-culture of BM-MSCs with endothelial progenitor cells[71] or umbilical endothelial cells.[72] However, there is still some controversy in the ability of

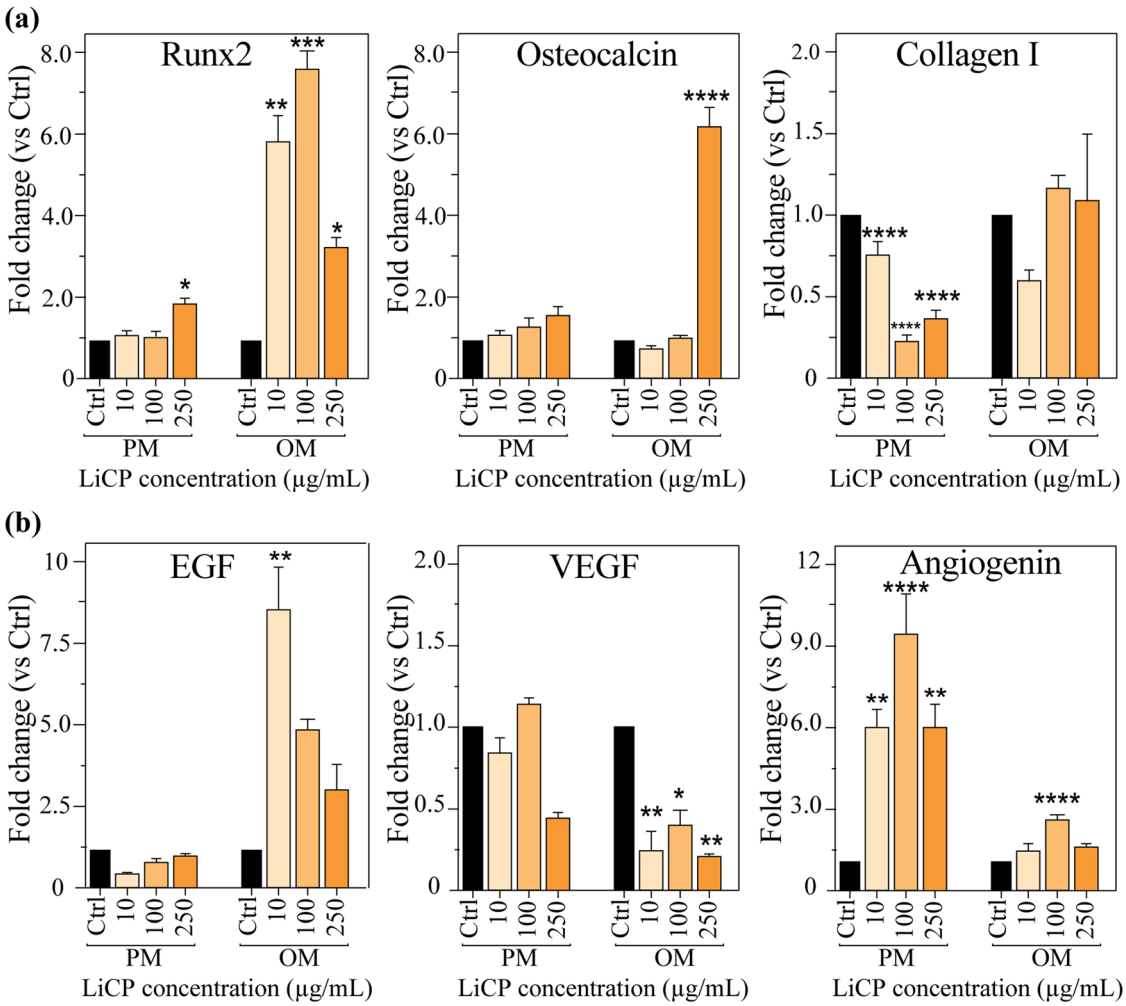

Fig. 5 (a) Osteogenic marker gene expression of Runx2, osteocalcin, and collagen I (col. I) compared to control cells. (b) Angiogenic marker expression of EGF (i), VEGF (ii) and angiogenin (iii) compared to control cells. *$p < 0.02$, **$p < 0.01$, ***$p < 0.001$, ****$p < 0.0001$.

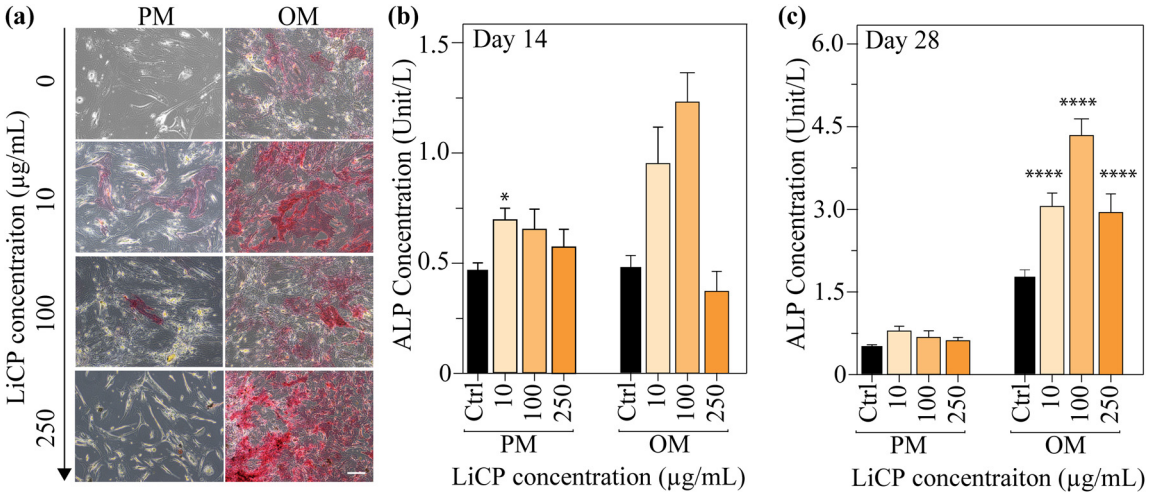

Fig. 6 Representative images of ALP staining in BM-MSCs cultured at different concentrations of LiCP, after 28 days (a) and ALP activity of samples under the same conditions at day 14 (b) and 28 (c). Scale bar: 100 μm. *$p < 0.02$, **$p < 0.01$, ***$p < 0.001$, ****$p < 0.0001$.

BM-MSCs ability to differentiate into functional endothelial cells. There is clear evidence that the release of paracrine factors from mesenchymal stem cells contribute to vascular formation and function.[73] In addition, lithium has been demonstrated to not only stimulate the proliferation and differentiation of osteoblasts, but also to induce an increase of angiogenic factors.[71,74] To study the effect of conditioned media from cells in the presence of LiCP on vessel formation, we used an *in vitro* tubulogenesis assay using human endothelial cells (HMVECs). BM-MSCs were first cultured for up to 10 days in the presence of nanoparticles at different concentrations, either in proliferation or endothelial medium (Fig. S6, ESI†). At a macroscopic observation, BM-MSCs did not show an influence in cell morphology when cultured in endothelial medium (Fig. 7a, i). Gene expression of samples collected after 7 days of culture showed significant increase of EGF of at least 2-folds, in cells cultured with LiCP, compared to the control (Fig. 7a, iii). Angiogenin was also up-regulated in cells cultured with 10 μg mL^{-1} LiCP. Exposure to 100 μg mL^{-1} LiCP did not show significant increase in angiogenin expression compared to the control (Fig. 7a, iv). Surprisingly, VEGF was down-regulated in 100 μg mL^{-1} Li-CaP (Fig. 7a, ii).

After 10 days of culture, conditioned media from each group were then collected and used to perform the tubulogenesis assay. Cells cultured in regular EGM were used as the negative control as they showed only very little tube formation, whereas cells in the same media with supplemented growth factors containing proangiogenic molecules, were used as a positive control (Fig. 7b). HMVEC morphology dramatically changed when cultured with different conditioned media, showing a pronounced tube formation in cells with 100 μg mL^{-1} LiCP and proliferation medium. All nanoparticle groups with proliferation medium showed significantly higher tubulogenesis than the negative control (Fig. 7b, ii). Tube formation of HMVEC performed with endothelial medium groups revealed enhanced tube formation in all groups treated with LiCP, with 10 and 100 μg mL^{-1} having significantly increased values (Fig. 7b, iii).

To further investigate LiCP capability in osteogenesis *in vivo*, the nanoparticles were embedded in collagen hydrogel at a concentration of 1 mg mL^{-1} and tested *in vivo* in an ectopic model. Collagen hydrogel and collagen embedded with ACP particles were used as controls. All groups were combined with BMSCs to facilitate tumor formation (Fig. 8a). After five weeks, surprisingly, the collagen hydrogels and hydrogels containing LiCP showed formation of ectopic bone mass (Fig. 8a, bottom). Moreover, samples with LiCP presented a more uniform and dense bone formation compared to the control (Fig. 8b–d) and showed increased new bone area. Masson's trichrome staining also showed a significant increase in new bone area in LiCP compared to the control and notably particles had been resorbed.

Notably, hydrogels containing LiCP were the only group that showed mature bone formation, highly suggesting that LiCP helped form vascularization at the early stage and allowed the formation of uniform bone. Lithium has a complex but significant role in osteogenesis, influencing various cellular processes related to bone formation and repair. It has been demonstrated that lithium chloride can stimulate bone formation by enhancing alkaline phosphatase activity, promoting the growth of mineralized nodules, and supporting osteogenic differentiation *in vitro*.[75] This effect is primarily mediated through the inhibition of GSK-3β, a key component in the Wnt signaling pathway, which is crucial for bone development and maintenance. Our gene expression results showed an upregulation of Runx2, indicative of Wnt signaling involvement, as it is one of the downstream genes of this pathway.[76] However, it has also been observed that the effects of lithium on osteogenesis can vary depending on the dosage, cellular context and the specific stages of cell maturation. For example, prolonged treatment with lithium chloride has shown to inhibit osteoblast differentiation in more mature cells of the dental

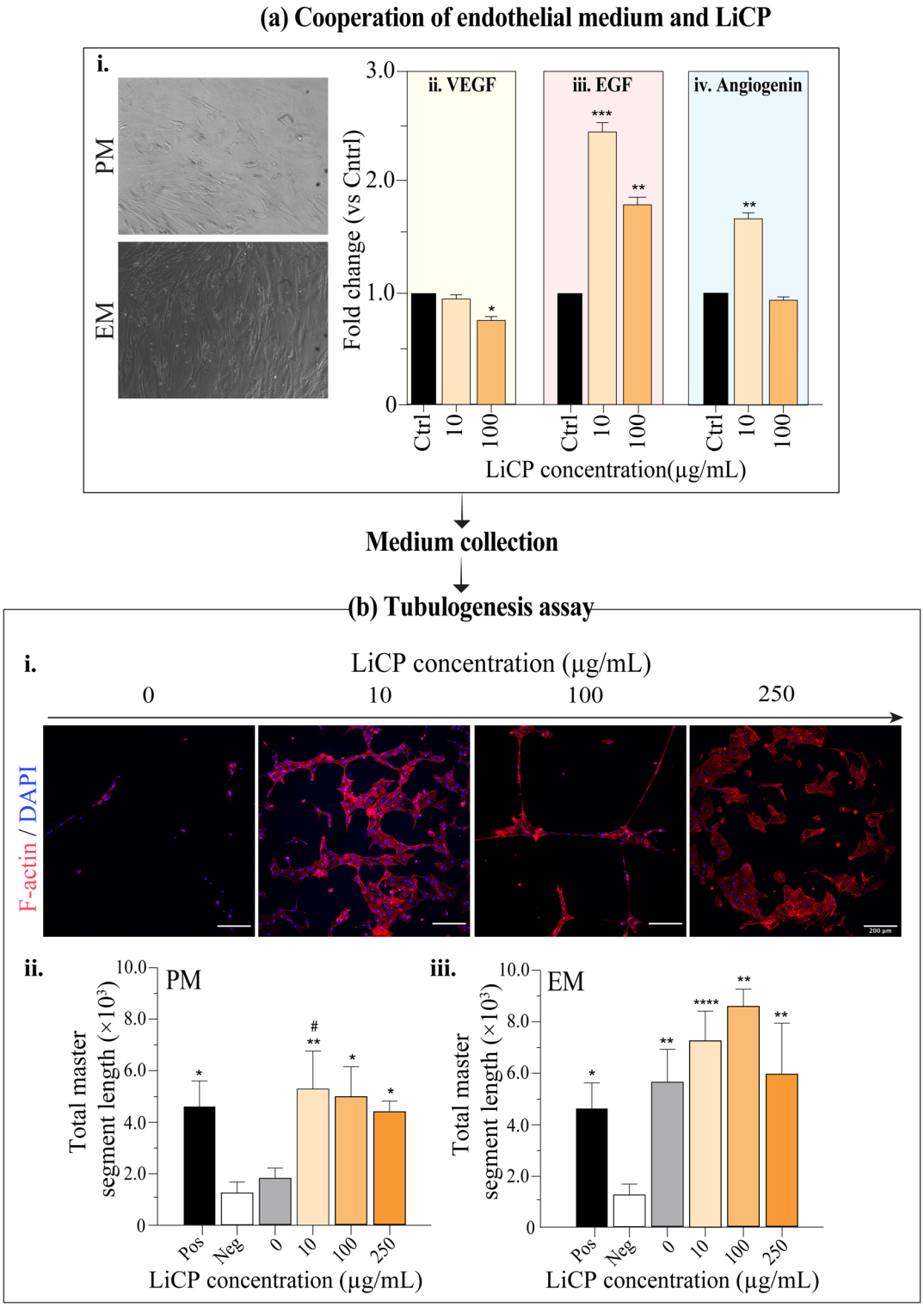

Fig. 7 (a) Representative images of BM-MSCs cultured in proliferation (i, top) *vs.* endothelial (medium (i, down). Gene expression of VEGF (ii), EGF (iii), and angiogenin (iv), of cells cultured in endothelial medium in combination with LiCP; (b) effect of BM-MSC conditioned media on HMVEC tubulogenesis. (i) F-actin (red) and DAPI (blue) staining of HMVECs cultured with each conditioned media (scale bar: 200 μm); tubulogenesis quantitative measurement of samples in proliferation (ii) and endothelial (iii) medium. Pos: EGM fully supplemented medium; Neg: regular EGM-2 medium; *$p < 0.02$, **$p < 0.01$, ***$p < 0.001$, ****$p < 0.0001$ (*vs.* Neg); # $p < 0.02$ (*vs.* group without nanoparticle "0").

pulp, indicating that its effects might be differential and dependent on the developmental stage of the cells involved or highly dose dependent.[77] Additionally, studies have suggested that while lithium enhances osteogenesis, it may also modulate

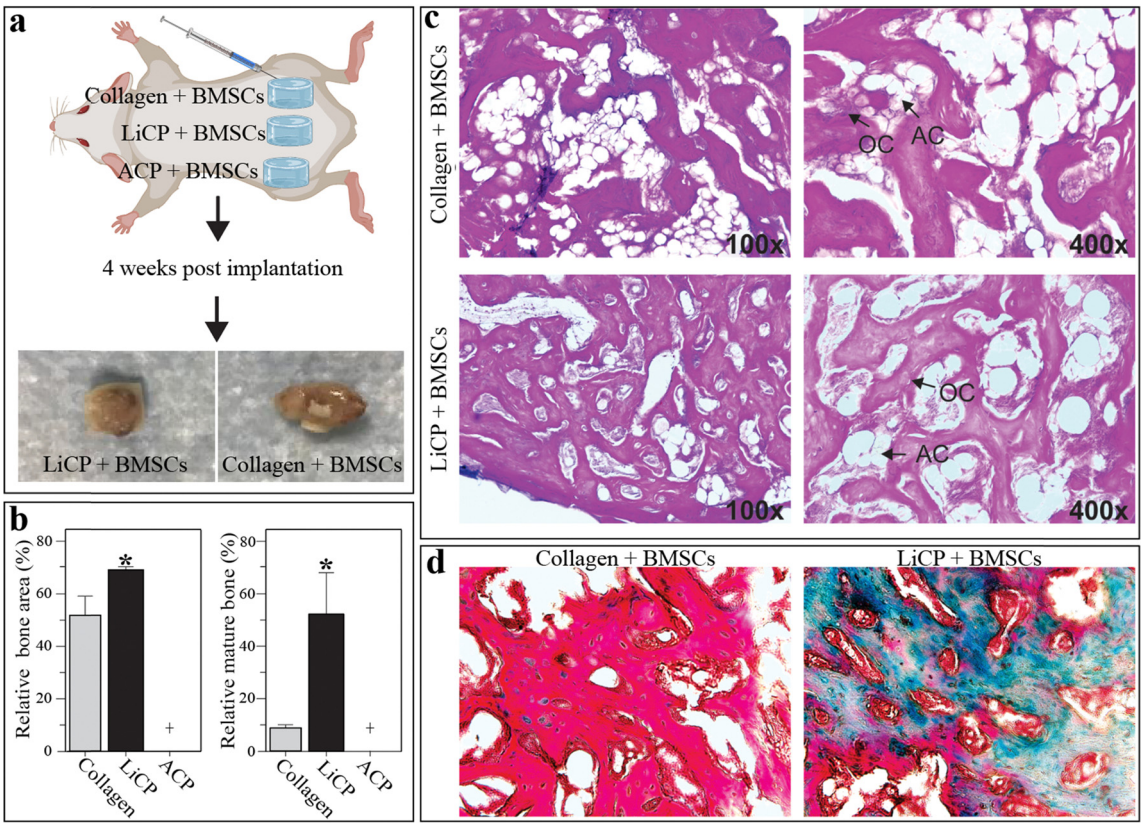

Fig. 8 *In vivo* bone formation. (a) Top: schematic of the *in vivo* experimental set up and study groups, bottom: images of bone mass formed in the control group (collagen hydrogel + BMSCs) and collage hydrogel containing 1 mg mL^{-1} LiCP + BMSCs. The collagen hydrogels containing ACP + BMSCs did not form bone mass. (b) Quantification of histological sections for relative bone area and mature bone. (c) Representative images of hematoxylin & eosin (H & E) staining. Representative osteocyte (OC) and adipocyte (AC) are indicated by arrows. (d) Images of Masson's trichrome staining. *$p < 0.02$.

adipogenesis, potentially influencing the balance between these two processes in bone marrow-derived mesenchymal stem cells.[78] The influence of lithium when combined with calcium phosphates on osteogenic differentiation has been reported. Lithium ions can significantly enhance the osteogenic properties of calcium phosphate materials, as Yoo *et al.* demonstrated when they explored how lithium doped into biphasic calcium phosphate can modify its crystal structure and improve its biological responses, thereby enhancing its osteogenic potential. However these are not fully resorbable as biphasic calcium contains crystalline hydroxyapatite.[79] Our *in vivo* data is indicative of the resorbability of LiCP and formation of ectopic mature bone. This is particularly significant in bone tissue engineering, where most bioactive calcium phosphate compositions are not fully resorbable while at the same time can significantly influence bone regeneration and repair. In addition to improving restorability, the introduction of lithium ions into amorphous calcium phosphate enhanced the material's ability to stimulate bone formation. Lithium has also been identified as a promoter for vascularization. Lithium can enhance vascularization through the expression of vascular endothelial growth factor (VEGF) and other angiogenic factors, which are crucial for new tissue formation and healing in bone regeneration processes. Cao *et al.* developed calcium sulfate-based bone cement doped with nanoporous lithium doping magnesium silicate and demonstrated that lithium can significantly enhance both osteogenesis and vascularization. This is particularly evident in *in vivo* settings, where such materials were implanted into bone defects and showed improved vascular network formation alongside bone tissue regeneration. The addition of lithium appears to increase the expression of key osteogenic and angiogenic markers, suggesting a dual role in promoting bone density and enhancing blood vessel formation.[80] Our results align with previous results in the literature, confirming the importance of lithium ions. In conclusion, our findings suggest that LiCP nanoparticles could be highly beneficial in clinical applications involving bone repair and regeneration, where promoting vascularization and osteogenesis are essential for successful healing of bone defects.

4. Conclusion

In conclusion, this study successfully demonstrates the synthesis of lithiated amorphous calcium phosphate (LiCP) nanoparticles. LiCP can release lithium ions in a sustained and controlled dosage. The *in vitro* data highlight the exceptional biocompatibility of these nanoparticles at the range of concentrations tested by maintaining high cell viability. The LiCP can

induce significant osteogenic and angiogenic responses. *In vivo* study revealed that LiCP is resorbable and can promote ectopic bone formation. The lithiated nanoparticles present a highly promising material for advancing bone repair and regeneration therapies, offering dual benefits in osteogenesis and angiogenesis. These findings lay the groundwork for future studies and potential clinical applications, where precise modulation of lithium release could tailor therapeutic outcomes to meet specific patient needs in bone and vascular tissue engineering. These findings establish a strong foundation for future research and potential clinical applications involving LiCP, where the precise modulation of lithium release could be tailored to achieve specific therapeutic outcomes in bone and vascular tissue engineering. Future studies can aim to explore molecular pathways to strengthen the link between phenotypic outcomes and molecular changes.

Data availability

The data supporting the findings of this study are available upon reasonable request.

Conflicts of interest

There are no conflicts to declare.

Acknowledgements

The authors would like to acknowledge the Australian National Health and Medical Research Council (Grant No. GNT1111694 and GNT1141602), and Sydney Musculoskeletal Health. The reported work was also supported in part by research grants from the National Institutes of Health (CA226303 and DE030480). This project used the core facilities that were supported in part by The University of Chicago Cancer Center Support Grant (P30CA014599) and the National Center for Advancing Translational Sciences (NCATS) of the National Institutes of Health through Grant Number 5UL1TR002389. TCH was supported by the Mabel Green Myers Research Endowment Fund and The University of Chicago Orthopaedics Alumni Fund. Funding sources were not involved in the study design, in the collection, analysis and interpretation of data, in the writing of the report, and in the decision to submit the paper for publication.

References

1 Z. J. Balogh, M. K. Reumann, R. L. Gruen, P. Mayer-Kuckuk, M. A. Schuetz and I. A. Harris, *et al.*, Advances and future directions for management of trauma patients with musculoskeletal injuries, *Lancet*, 2012, **380**(9847), 1109–1119. Available from: **https://www.scopus.com/inward/record.uri?eid=2-s2.0-84866481230&doi=10.1016%2FS0140-6736%2812%2960991-X&partnerID=40&md5=590ad13bd00691af6ba8ba557156ae2b**.

2 M. Vallet-Regí and E. Ruiz-Hernández, Bioceramics: From Bone Regeneration to Cancer Nanomedicine, *Adv. Mater.*, 2011, **23**(44), 5177–5218, DOI: **10.1002/adma.201101586**.

3 J. Zhou, Z. Zhang, J. Joseph, X. Zhang, B. E. Ferdows and D. N. Patel, *et al.*, Biomaterials and nanomedicine for bone regeneration: Progress and future prospects, *Exploration*, 2021, **1**(2), 20210011. Available from: **https://www.scopus.com/inward/record.uri?eid=2-s2.0-85177782177&doi=10.1002%2FEXP.20210011&partnerID=40&md5=b13da017d287c377c49cfc77926d01a0**.

4 W. Qiao, H. Xie, J. Fang, J. Shen, W. Li and D. Shen, *et al.*, Sequential activation of heterogeneous macrophage phenotypes is essential for biomaterials-induced bone regeneration, *Biomaterials*, 2021, **276**, 121038.

5 R. Hänsch and R. R. Mendel, Physiological functions of mineral micronutrients (Cu, Zn, Mn, Fe, Ni, Mo, B, Cl), *Curr. Opin. Plant Biol.*, 2009, **12**(3), 259–266. Available from: **https://www.scopus.com/inward/record.uri?eid=2-s2.0-66949153985&doi=10.1016%2Fj.pbi.2009.05.006&partnerID=40&md5=b45b5db510516bc5050b63de6a214b6d**.

6 E. Jakobsson, O. Argüello-Miranda, S.-W. Chiu, Z. Fazal, J. Kruczek and S. Nunez-Corrales, *et al.*, Towards a Unified Understanding of Lithium Action in Basic Biology and its Significance for Applied Biology, *J. Membr. Biol.*, 2017, **250**(6), 587–604. Available from: **https://www.scopus.com/inward/record.uri?eid=2-s2.0-85033453121&doi=10.1007%2Fs00232-017-9998-2&partnerID=40&md5=d8e6b983c6a366e6cb17acf7f9f307e1**.

7 C. Yang, W. Wang, K. Zhu, W. Liu, Y. Luo and X. Yuan, *et al.*, Lithium chloride with immunomodulatory function for regulating titanium nanoparticle-stimulated inflammatory response and accelerating osteogenesis through suppression of MAPK signaling pathway, *Int. J. Nanomed.*, 2019, **14**, 7475–7488.

8 K. Sakrajda and A. Szczepankiewicz, Inflammation-related changes in mood disorders and the immunomodulatory role of Lithium, *Int. J. Mol. Sci.*, 2021, **22**(4), 1–15. Available from: **https://www.scopus.com/inward/record.uri?eid=2-s2.0-85100234305&doi=10.3390%2Fijms22041532&partnerID=40&md5=27b410986e5a13353b6bf3c7f33ab088**.

9 F. Peng, L. Qiu, M. Yao, L. Liu, Y. Zheng and S. Wu, *et al.*, A lithium-doped surface inspires immunomodulatory functions for enhanced osteointegration through PI3K/AKT signaling axis regulation, *Biomater. Sci.*, 2021, **9**(24), 8202–8220. Available from: **https://www.scopus.com/inward/record.uri?eid=2-s2.0-85121045410&doi=10.1039%2Fd1bm01075a&partnerID=40&md5=1b883ff2f06582e3f56d413763e30386**.

10 L. Huang, X. Yin, J. Chen, R. Liu, X. Xiao and Z. Hu, *et al.*, Lithium chloride promotes osteogenesis and suppresses apoptosis during orthodontic tooth movement in osteoporotic model via regulating autophagy, *Bioact. Mater.*, 2021, **6**(10), 3074–3084. Available from: **https://www.scopus.com/inward/record.uri?eid=2-s2.0-85102118817&doi=10.1016%2Fj.bioactmat.2021.02.015&partnerID=40&md5=44ec03d6f4f7ac2397be9e0c5b085675**.

11 N. Salam and I. R. Gibson, Lithium ion doped carbonated hydroxyapatite compositions: Synthesis, physicochemical

characterisation and effect on osteogenic response in vitro, *Biomater. Adv.*, 2022, **140**, 213068. Available from: https://www.scopus.com/inward/record.uri?eid=2-s2.0-85135684657&doi=10.1016%2Fj.bioadv.2022.213068&partnerID=40&md5=ead22ba6117616d39073c1189810a02c.

12 S. K. Wong, K.-Y. Chin and S. Ima-Nirwana, The Skeletal-Protecting Action and Mechanisms of Action for Mood-Stabilizing Drug Lithium Chloride: Current Evidence and Future Potential Research Areas, *Front. Pharmacol.*, 2020, **11**, 430. Available from: https://www.scopus.com/inward/record.uri?eid=2-s2.0-85083520007&doi=10.3389%2Ffphar.2020.00430&partnerID=40&md5=b08e95fc320a6868123433b3e1cbbdd6.

13 A. Thorfve, A. Bergstrand, K. Ekström, A. Lindahl, P. Thomsen and A. Larsson, *et al.*, Gene expression profiling of peri-implant healing of PLGA-Li+ implants suggests an activated Wnt signaling pathway *in vivo*, *PLoS One*, 2014, **9**(7), e102597. Available from: https://www.scopus.com/inward/record.uri?eid=2-s2.0-84904576603&doi=10.1371%2Fjournal.pone.0102597&partnerID=40&md5=40cfbae4f9cdfaea874a6ee4b0bf7bb3.

14 J. Zhang, L. Cai, L. Tang, X. Zhang, L. Yang and K. Zheng, *et al.*, Highly dispersed lithium doped mesoporous silica nanospheres regulating adhesion, proliferation, morphology, ALP activity and osteogenesis related gene expressions of BMSCs, *Colloids Surf., B*, 2018, **170**, 563–571. Available from: https://www.scopus.com/inward/record.uri?eid=2-s2.0-85049302515&doi=10.1016%2Fj.colsurfb.2018.06.038&partnerID=40&md5=d86e5cdb7acad7b3202f405fdf74ae7a.

15 M. Arioka, F. Takahashi-Yanaga, M. Sasaki, T. Yoshihara, S. Morimoto and M. Hirata, *et al.*, Acceleration of bone regeneration by local application of lithium: Wnt signal-mediated osteoblastogenesis and Wnt signal-independent suppression of osteoclastogenesis, *Biochem. Pharmacol.*, 2014, **90**(4), 397–405. Available from: https://www.scopus.com/inward/record.uri?eid=2-s2.0-84907053266&doi=10.1016%2Fj.bcp.2014.06.011&partnerID=40&md5=ba2dbe4bab1574142f8590048beb0787.

16 T. Pepersack, J. Corvilain and P. Bergmann, Effects of lithium on bone resorption in cultured foetal rat long-bones, *Eur. J. Clin. Invest.*, 1994, **24**(6), 400–405. Available from: https://www.scopus.com/inward/record.uri?eid=2-s2.0-0028352121&doi=10.1111%2Fj.1365-2362.1994.tb02183.x&partnerID=40&md5=f9818b1799c997c3692f1cf9026113ad.

17 M. Khorami, S. Hesaraki, A. Behnamghader, H. Nazarian and S. Shahrabi, In vitro bioactivity and biocompatibility of lithium substituted 45S5 bioglass, *Mater. Sci. Eng., C*, 2011, **31**(7), 1584–1592, DOI: 10.1016/j.msec.2011.07.011.

18 P. Han, C. Wu, J. Chang and Y. Xiao, The cementogenic differentiation of periodontal ligament cells via the activation of Wnt/β-catenin signalling pathway by Li + ions released from bioactive scaffolds, *Biomaterials*, 2012, **33**(27), 6370–6379, DOI: 10.1016/j.biomaterials.2012.05.061.

19 Y. Wu, S. Zhu, C. Wu, P. Lu, C. Hu and S. Xiong, *et al.*, A Bi-lineage conducive scaffold for osteochondral defect regeneration, *Adv. Funct. Mater.*, 2014, **24**(28), 4473–4483.

20 C. Pan, L. Chen, R. Wu, H. Shan, Z. Zhou and Y. Lin, *et al.*, Lithium-containing biomaterials inhibit osteoclastogenesis of macrophages: In vitro and osteolysis *in vivo*, *J. Mater. Chem. B*, 2018, **6**(48), 8115–8126.

21 D. Li, L. Huifang, J. Zhao, Z. Yang, X. Xie and Z. Wei, *et al.*, Porous lithium-doped hydroxyapatite scaffold seeded with hypoxia-preconditioned bone-marrow mesenchymal stem cells for bone-tissue regeneration, *Biomed. Mater.*, 2018, **13**(5), 055002. Available from: https://www.scopus.com/inward/record.uri?eid=2-s2.0-85051948223&doi=10.1088%2F1748-605X%2Faac627&partnerID=40&md5=4a824c28e9e4fea0f633842b19535332.

22 L. Liu, Y. Liu, C. Feng, J. Chang, R. Fu and T. Wu, *et al.*, Lithium-containing biomaterials stimulate bone marrow stromal cell-derived exosomal miR-130a secretion to promote angiogenesis, *Biomaterials*, 2019, **192**, 523–536. Available from: https://www.scopus.com/inward/record.uri?eid=2-s2.0-85059309544&doi=10.1016%2Fj.biomaterials.2018.11.007&partnerID=40&md5=cc70e86a21a9cfa10d0eda5eb71d35eb.

23 L. A. Haro Durand, G. E. Vargas, R. Vera-Mesones, A. Baldi, M. P. Zago and M. A. Fanovich, *et al.*, In vitro human umbilical vein endothelial cells response to ionic dissolution products from lithium-containing 45S5 bioactive glass, *Materials*, 2017, **10**(7), 740.

24 X. Zhang, K. Nan, Y. Zhang, K. Song, Z. Geng and D. Shang, *et al.*, Lithium and cobalt co-doped mesoporous bioactive glass nanoparticles promote osteogenesis and angiogenesis in bone regeneration, *Front. bioeng. biotechnol.*, 2023, **11**, 1288393. Available from: https://www.scopus.com/inward/record.uri?eid=2-s2.0-85182405513&doi=10.3389%2Ffbioe.2023.1288393&partnerID=40&md5=3c57f67f31ed0d0dc7642b44ec0d7f8c.

25 T.-L. Lin, Y.-H. Lin, A. K.-X. Lee, T.-Y. Kuo, C.-Y. Chen and K.-H. Chen, *et al.*, The exosomal secretomes of mesenchymal stem cells extracted via 3D-printed lithium-doped calcium silicate scaffolds promote osteochondral regeneration, *Mater. Today Bio*, 2023, **22**, 100728. Available from: https://www.scopus.com/inward/record.uri?eid=2-s2.0-85166021166&doi=10.1016%2Fj.mtbio.2023.100728&partnerID=40&md5=ee67887ce56b2b91121eca34e47dad2e.

26 F. He, X. Yuan, T. Lu, Y. Wang, S. Feng and X. Shi, *et al.*, Preparation and characterization of novel lithium magnesium phosphate bioceramic scaffolds facilitating bone generation, *J. Mater. Chem. B*, 2022, **10**(21), 4040–4047. Available from: https://www.scopus.com/inward/record.uri?eid=2-s2.0-85131217772&doi=10.1039%2Fd2tb00471b&partnerID=40&md5=860383fd2a248b283abd12533a0869a4.

27 Z. Wu, J. Bai, G. Ge, T. Wang, S. Feng and Q. Ma, *et al.*, Regulating Macrophage Polarization in High Glucose Microenvironment Using Lithium-Modified Bioglass-Hydrogel for Diabetic Bone Regeneration, *Adv. Healthcare Mater.*, 2022, **11**(13), 2200298. Available from: https://www.scopus.com/inward/record.uri?eid=2-s2.0-85128190240&doi=10.1002%2Fadhm.202200298&partnerID=40&md5=ed626c35ad657dea2f8cef7e3497eec9.

28 Y. Luo, H. Liu, Y. Zhang, Y. Liu, S. Liu and X. Liu, *et al.*, Metal ions: the unfading stars of bone regeneration—from bone metabolism regulation to biomaterial applications., *Biomater. Sci.*, 2023, **11**(22), 7268–7295. Available from: https://www.scopus.com/inward/record.uri?eid=2-s2.0-85174545750&doi=10.1039%2Fd3bm01146a&partnerID=40&md5=522117fe85090f31d677ad8ee98ec8ca.

29 C. Qin, J. Ma, L. Chen, H. Ma, H. Zhuang and M. Zhang, *et al.*, 3D bioprinting of multicellular scaffolds for osteochondral regeneration, *Mater. Today*, 2021, **49**, 68–84. Available from: https://www.scopus.com/inward/record.uri?eid=2-s2.0-85106263060&doi=10.1016%2Fj.mattod.2021.04.016&partnerID=40&md5=7e461a93b3922ddb700db4191b828f2e.

30 L. Liu, F. Yu, L. Chen, L. Xia, C. Wu and B. Fang, Lithium-Containing Biomaterials Stimulate Cartilage Repair through Bone Marrow Stromal Cells-Derived Exosomal miR-455-3p and Histone H3 Acetylation, *Adv. Healthcare Mater.*, 2023, **12**(11), 2202390. Available from: https://www.scopus.com/inward/record.uri?eid=2-s2.0-85147012617&doi=10.1002%2Fadhm.202202390&partnerID=40&md5=481f4b8be20c1102ce750a0bbce65af0.

31 L. Chen, C. Deng, J. Li, Q. Yao, J. Chang and L. Wang, *et al.*, 3D printing of a lithium-calcium-silicate crystal bioscaffold with dual bioactivities for osteochondral interface reconstruction, *Biomaterials*, 2018, 1–13. Available from: https://linkinghub.elsevier.com/retrieve/pii/S0142961218302448.

32 Q. Zhang, L. Chen, B. Chen, C. Chen, J. Chang and Y. Xiao, *et al.*, Lithium-calcium-silicate bioceramics stimulating cementogenic/osteogenic differentiation of periodontal ligament cells and periodontal regeneration, *Appl. Mater. Today*, 2019, **16**, 375–387. Available from: https://www.scopus.com/inward/record.uri?eid=2-s2.0-85070089076&doi=10.1016%2Fj.apmt.2019.06.011&partnerID=40&md5=7e51557e6c5df11c6a75a9fc9cf7fb12.

33 W. Wang, J. Wei, D. Lei, S. Wang, B. Zhang and S. Shang, *et al.*, 3D printing of lithium osteogenic bioactive composite scaffold for enhanced bone regeneration, *Composites, Part B*, 2023, **256**, 110641. Available from: https://www.scopus.com/inward/record.uri?eid=2-s2.0-85150840391&doi=10.1016%2Fj.compositesb.2023.110641&partnerID=40&md5=d12a752d9225befd99f4708564735eb8.

34 Y. Luo, Z. Yang, X. Zhao, D. Li, Q. Li and Y. Wei, *et al.*, Immune regulation enhances osteogenesis and angiogenesis using an injectable thiolated hyaluronic acid hydrogel with lithium-doped nano-hydroxyapatite (Li-nHA) delivery for osteonecrosis, *Mater. Today Bio*, 2024, **25**, 100976. Available from: https://www.scopus.com/inward/record.uri?eid=2-s2.0-85183881977&doi=10.1016%2Fj.mtbio.2024.100976&partnerID=40&md5=e73efd4706e2638fc6a6fb65bd56704c.

35 M. Kaasalainen, R. Zhang, P. Vashisth, A. A. Birjandi, M. S'Ari and D. A. Martella, *et al.*, Lithiated porous silicon nanowires stimulate periodontal regeneration, *Nat. Commun.*, 2024, **15**(1), 487. Available from: https://www.scopus.com/inward/record.uri?eid=2-s2.0-85182177983&doi=10.1038%2Fs41467-023-44581-5&partnerID=40&md5=a07afa8913490791017084ba9bc1c195.

36 K. Zhang, Z. Jia, B. Yang, Q. Feng, X. Xu and W. Yuan, *et al.*, Adaptable Hydrogels Mediate Cofactor-Assisted Activation of Biomarker-Responsive Drug Delivery via Positive Feedback for Enhanced Tissue Regeneration, *Adv. Sci.*, 2018, **5**(12), 1800875.

37 R. Yang, G. Li, C. Zhuang, P. Yu, T. Ye and Y. Zhang, *et al.*, Gradient bimetallic ion-based hydrogels for tissue microstructure reconstruction of tendon-to-bone insertion, *Sci. Adv.*, 2021, **7**(26), eabg3816.

38 C. Lu, L. Wang, L. Zhang, C. Xue, H. Ye and X. Chen, *et al.*, Li-doped calcium phosphate cement for accelerated bone regeneration of osteoporotic bone defect, *J. Appl. Biomater. Funct. Mater.*, 2022, **20**, DOI: 10.1177/22808000221099012. Available from: https://www.scopus.com/inward/record.uri?eid=2-s2.0-85138397109&doi=10.1177%2F22808000221099012&partnerID=40&md5=3bba2c98d27f4e74d70aa67ec0c81b93.

39 C. Liang, Q. Jiang, Y. Yu, T. Xu, H. Sun and F. Deng, *et al.*, Antibacterial Evaluation of Lithium-Loaded Nanofibrous Poly(L-Lactic Acid) Membranes Fabricated via an Electrospinning Strategy, *Front. Bioeng. Biotechnol.*, 2021, **9**, 676874. Available from: https://www.scopus.com/inward/record.uri?eid=2-s2.0-85105947103&doi=10.3389%2Ffbioe.2021.676874&partnerID=40&md5=314bf3c653bb1ba107ed5713e2ef424d.

40 V. Miguez-Pacheco, T. Büttner, A. L. B. Maçon, J. R. Jones, T. Fey and D. De Ligny, *et al.*, Development and characterization of lithium-releasing silicate bioactive glasses and their scaffolds for bone repair, *J. Non-Cryst. Solids*, 2016, **432**, 65–72, DOI: 10.1016/j.jnoncrysol.2015.03.027.

41 M. Mousa, J. A. Milan, O. Kelly, J. Doyle, N. D. Evans and R. O. C. Oreffo, *et al.*, The role of lithium in the osteogenic bioactivity of clay nanoparticles., *Biomater. Sci.*, 2021, **9**(8), 3150–3161. Available from: https://www.scopus.com/inward/record.uri?eid=2-s2.0-85104614889&doi=10.1039%2Fd0bm01444c&partnerID=40&md5=47f42c674c6c9368f39c20bc39623303.

42 R. R. Mendel, A. G. Smith, A. Marquet and M. J. Warren, Metal and cofactor insertion, *Nat. Prod. Rep.*, 2007, **24**(5), 963–971. Available from: https://www.scopus.com/inward/record.uri?eid=2-s2.0-34848918221&doi=10.1039%2Fb703112m&partnerID=40&md5=36595a8b1fd3b1e10eb1b081dfd2dc0f.

43 W. Wang, L. P. Billen and Y. Li, Sequence diversity, metal specificity, and catalytic proficiency of metal-dependent phosphorylating DNA enzymes, *Chem. Biol.*, 2002, **9**(4), 507–517. Available from: https://www.scopus.com/inward/record.uri?eid=2-s2.0-0036235747&doi=10.1016%2FS1074-5521%2802%2900127-8&partnerID=40&md5=5c41941a2fcba2065aab6e3acb0e3d02.

44 K. Placek, J. L. Schultze and A. C. Aschenbrenner, Epigenetic reprogramming of immune cells in injury, repair, and resolution, *J. Clin. Invest.*, 2019, **129**(8), 2994–3005. Available from: https://www.scopus.com/inward/record.uri?eid=2-s2.0-85070613920&doi=10.1172%2FJCI124619&partnerID=40&md5=dcc22cc4712948cc4423144368e9a898.

45 R. Whitaker, B. Hernaez-Estrada, R. M. Hernandez, E. Santos-Vizcaino and K. L. Spiller, Immunomodulatory Biomaterials for Tissue Repair, *Chem. Rev.*, 2021, **121**(18), 11305–11335. Available from: https://www.scopus.com/inward/record.uri?eid=2-s2.0-85114432723&doi=10.1021%2Facs.chemrev.0c00895&partnerID=40&md5=93a505bcabec7ffb361ced94ec6dca35.

46 C. Wang, R. Zhang, X. Wei, M. Lv and Z. Jiang, Metalloimmunology: The metal ion-controlled immunity, *Adv. Immunol.*, 2020, **145**, 187–241. Available from: https://www.scopus.com/inward/record.uri?eid=2-s2.0-85076611234&doi=10.1016%2Fbs.ai.2019.11.007&partnerID=40&md5=5521215eb2ff86b2d1191fbbc97c739d.

47 Z. Li, H. Wang, K. Zhang, B. Yang, X. Xie and Z. Yang, *et al.*, Bisphosphonate-based hydrogel mediates biomimetic negative feedback regulation of osteoclastic activity to promote bone regeneration, *Bioact. Mater.*, 2022, **13**, 9–22.

48 X. Chen, B. Tan, S. Wang, R. Tang, Z. Bao and G. Chen, *et al.*, Rationally designed protein cross-linked hydrogel for bone regeneration via synergistic release of magnesium and zinc ions, *Biomaterials*, 2021, 274.

49 Q. Huang, Z. Ouyang, Y. Tan, H. Wu and Y. Liu, Activating macrophages for enhanced osteogenic and bactericidal performance by Cu ion release from micro/nano-topographical coating on a titanium substrate, *Acta Biomater.*, 2019, **100**, 415–426.

50 M. Bartnikowski, H.-J. Moon and S. Ivanovski, Release of lithium from 3D printed polycaprolactone scaffolds regulates macrophage and osteoclast response, *Biomed. Mater.*, 2018, **13**(6), 065003.

51 C. Jagannathan, R. Waddington and W. Nishio Ayre, Nanoparticle and Nanotopography-Induced Activation of the Wnt Pathway in Bone Regeneration, *Tissue Eng., Part B*, 2024, **30**(2), 270–283. Available from: https://www.scopus.com/inward/record.uri?eid=2-s2.0-85179396554&doi=10.1089%2Ften.teb.2023.0108&partnerID=40&md5=632a05e7331187bd3d4057314c2c9454.

52 E. Huang, Y. Bi, W. Jiang, X. Luo, K. Yang and J. L. Gao, *et al.*, Conditionally immortalized mouse embryonic fibroblasts retain proliferative activity without compromising multipotent differentiation potential, *PLoS One*, 2012, **7**(2), 1–11.

53 Y. Li, E. R. Wagner, Z. Yan, Z. Wang, G. Luther and W. Jiang, *et al.*, The calcium-binding protein S100A6 accelerates human osteosarcoma growth by promoting cell proliferation and inhibiting osteogenic differentiation, *Cell. Physiol. Biochem.*, 2015, **37**(6), 2375–2392.

54 F. Deng, X. Chen, Z. Liao, Z. Yan, Z. Wang and Y. Deng, *et al.*, A simplified and versatile system for the simultaneous expression of multiple siRNAs in mammalian cells using gibson DNA assembly, *PLoS One*, 2014, **9**(11), 1–12.

55 J. Liao, Q. Wei, Y. Zou, J. Fan, D. Song and J. Cui, *et al.*, Notch signaling augments BMP9-induced bone formation by promoting the osteogenesis-angiogenesis coupling process in Mesenchymal Stem Cells (MSCs), *Cell. Physiol. Biochem.*, 2017, **41**(5), 1905–1923.

56 C. Zhao, Z. Zeng, N. T. Qazvini, X. Yu, R. Zhang and S. Yan, *et al.*, Thermoresponsive Citrate-Based Graphene Oxide Scaffold Enhances Bone Regeneration from BMP9-Stimulated Adipose-Derived Mesenchymal Stem Cells, *ACS Biomater. Sci. Eng.*, 2018, **4**(8), 2943–2955.

57 Y. Su, E. R. Wagner, Q. Luo, J. Huang, L. Chen and B. C. He, *et al.*, Insulin-like growth factor binding protein 5 suppresses tumor growth and metastasis of human osteosarcoma, *Oncogene*, 2011, **30**(37), 3907–3917.

58 J. Wang, H. Zhang, W. Zhang, E. Huang, N. Wang and N. Wu, *et al.*, Bone morphogenetic protein-9 effectively induces osteo/odontoblastic differentiation of the reversibly immortalized stem cells of dental apical papilla, *Stem Cells Dev.*, 2014, **23**(12), 1405–1416.

59 J. Ye, J. Wang, Y. Zhu, Q. Wei, X. Wang and J. Yang, *et al.*, A thermoresponsive polydiolcitrate-gelatin scaffold and delivery system mediates effective bone formation from BMP9-transduced mesenchymal stem cells, *Biomed. Mater.*, 2016, **11**(2), 025021.

60 H. Zhang, J. Wang, F. Deng, E. Huang, Z. Yan and Z. Wang, *et al.*, Canonical Wnt signaling acts synergistically on BMP9-induced osteo/odontoblastic differentiation of stem cells of dental apical papilla (SCAPs), *Biomaterials*, 2015, **39**, 145–154.

61 Y. G. Zhu, Q. Liu, Y. Rong, H. Chen, J. Yang and C. Jia, *et al.*, Proton enhanced dynamic battery chemistry for aprotic lithium–oxygen batteries, *Nat. Commun.*, 2017, **8**(1), 14308, DOI: 10.1038/ncomms14308.

62 V. S. Gorelik, A. I. Vodchits, D. Bi, V. V. Koltashev and V. G. Plotnichenko, Raman Scattering in LiOH and LiOD Polycrystals, *Inorg. Mater.*, 2019, **55**(3), 271–276, DOI: 10.1134/S0020168519030087.

63 S. F. Parker, K. Refson, R. I. Bewley and G. Dent, Assignment of the vibrational spectra of lithium hydroxide monohydrate, $LiOH{\cdot}H_2O$, *J. Chem. Phys.*, 2011, **134**(8), 84503, DOI: 10.1063/1.3553812.

64 V. S. Gorelik, D. Bi, Y. P. Voinov, A. I. Vodchits, B. P. Gorshunov and N. I. Yurasov, *et al.*, Raman spectra of lithium compounds, *J. Phys.: Conf. Ser.*, 2017. Available from: https://www.scopus.com/inward/record.uri?eid=2-s2.0-85037810042&doi=10.1088%2F1742-6596%2F918%2F1%2F012035&partnerID=40&md5=bd7d574cbf5301a02460d118d2b63bb8.

65 C. Freese, D. Schreiner, L. Anspach, C. Bantz, M. Maskos and R. E. Unger, *et al.*, In vitro investigation of silica nanoparticle uptake into human endothelial cells under physiological cyclic stretch, *Part. Fibre Toxicol.*, 2014, **11**(1), 1–12.

66 N. Kurgan, K. N. Bott, W. E. Helmeczi, B. D. Roy, I. D. Brindle and P. Klentrou, *et al.*, Low dose lithium supplementation activates Wnt/β-catenin signalling and increases bone OPG/RANKL ratio in mice, *Biochem. Biophys. Res. Commun.*, 2019, **511**(2), 394–397.

67 F. Matsuoka, I. Takeuchi, H. Agata, H. Kagami, H. Shiono and Y. Kiyota, *et al.*, Morphology-Based Prediction of Osteogenic Differentiation Potential of Human Mesenchymal Stem Cells, *PLoS One*, 2013, **8**(2), e55082. Available from: https://www.scopus.com/inward/record.uri?eid=2-s2.0-84874343832&doi=10.1371%2Fjournal.pone.0055082&partnerID=40&md5=e7d2d58b281f9b44e135906231d674d0.

68 M. F. Pittenger, A. M. Mackay, S. C. Beck, R. K. Jaiswal, R. Douglas and J. D. Mosca, *et al.*, Multilineage potential of adult human mesenchymal stem cells, *Science*, 1999, **284**(5411), 143–147. Available from: **https://www.scopus.com/inward/record.uri?eid=2-s2.0-0033515827&doi=10.1126%2Fscience.284.5411.143&partnerID=40&md5=ebf1520a8ee74941d6a11bc96169355e**.

69 K. Janeczek Portalska, A. Leferink, N. Groen, H. Fernandes, L. Moroni and C. van Blitterswijk, *et al.*, Endothelial Differentiation of Mesenchymal Stromal Cells, *PLoS One*, 2012, **7**(10), e46842. Available from: **https://www.scopus.com/inward/record.uri?eid=2-s2.0-84867123663&doi=10.1371%2Fjournal.pone.0046842&partnerID=40&md5=365e7d0216fa618a25f533f70d40ac28**.

70 C. Liu, A.-L. Tsai, P.-C. Li, C.-W. Huang and C.-C. Wu, Endothelial differentiation of bone marrow mesenchyme stem cells applicable to hypoxia and increased migration through Akt and NFκB signals, *Stem Cell Res. Ther.*, 2017, **8**(1), 1–11. Available from: **https://www.scopus.com/inward/record.uri?eid=2-s2.0-85011633160&doi=10.1186%2Fs13287-017-0470-0&partnerID=40&md5=450af75823ed56d2b3dc118c1818a558**.

71 T. Liang, L. Zhu, W. Gao, M. Gong, J. Ren and H. Yao, *et al.*, Coculture of endothelial progenitor cells and mesenchymal stem cells enhanced their proliferation and angiogenesis through PDGF and Notch signaling, *FEBS Open Bio*, 2017, **7**(11), 1722–1736. Available from: **https://www.scopus.com/inward/record.uri?eid=2-s2.0-85031495120&doi=10.1002%2F2211-5463.12317&partnerID=40&md5=6d9bdb69577517d80c140507b6e3db0e**.

72 J. Chen, L. Deng, C. Porter, G. Alexander, D. Patel and J. Vines, *et al.*, Angiogenic and Osteogenic Synergy of Human Mesenchymal Stem Cells and Human Umbilical Vein Endothelial Cells Cocultured on a Nanomatrix, *Sci. Rep.*, 2018, **8**(1), 15749. Available from: **https://www.scopus.com/inward/record.uri?eid=2-s2.0-85055460897&doi=10.1038%2Fs41598-018-34033-2&partnerID=40&md5=edc6606ca8d35143db8d4db56a474e53**.

73 S. M. Watt, F. Gullo, M. Van Der Garde, D. Markeson, R. Camicia and C. P. Khoo, *et al.*, The angiogenic properties of mesenchymal stem/stromal cells and their therapeutic potential, *Br. Med. Bull.*, 2013, **108**(1), 25–53. Available from: **https://www.scopus.com/inward/record.uri?eid=2-s2.0-84890034484&doi=10.1093%2Fbmb%2Fldt031&partnerID=40&md5=2b182083c6f9a6578ab4417bf54baac3**.

74 L. Li, X. Peng, Y. Qin, R. Wang, J. Tang and X. Cui, *et al.*, Acceleration of bone regeneration by activating Wnt/β-catenin signalling pathway via lithium released from lithium chloride/calcium phosphate cement in osteoporosis, *Sci. Rep.*, 2017, **7**, 45204. Available from: **https://www.scopus.com/inward/record.uri?eid=2-s2.0-85016156039&doi=10.1038%2Fsrep45204&partnerID=40&md5=76787d77543dcbf8e6f95f79160ed09f**.

75 Y. Bao, X. Lv, Y. Tang, X. Ru, J. Wang and J. Yan, *Lithium chloride enhances osteoblast differentiation and resists senile osteoporosis*, 2020.

76 C. Haxaire, E. Haÿ and V. Geoffroy, Runx2 Controls Bone Resorption through the Down-Regulation of the Wnt Pathway in Osteoblasts, *Am. J. Pathol.*, 2016, **186**(6), 1598–1609.

77 A. Vijaykumar and M. Mina, Lithium Chloride Exerts Differential Effects on Dentinogenesis and Osteogenesis in Primary Pulp Cultures, *Front. Dent. Med.*, 2021, **2**, 1–13.

78 L. Tang, Y. Chen, F. Pei and H. Zhang, Lithium chloride modulates adipogenesis and osteogenesis of human bone marrow-derived mesenchymal stem cells, *Cell. Physiol. Biochem.*, 2015, **37**(1), 143–152.

79 K. H. Yoo and Y. Kim, Kim Y Il, Bae MK, Yoon SY. Lithium doped biphasic calcium phosphate: Structural analysis and osteo/odontogenic potential in vitro, *Front. Bioeng. Biotechnol.*, 2022, **10**, 1–14.

80 L. Cao, W. Weng, X. Chen, J. Zhang, Q. Zhou and J. Cui, *et al.*, Promotion of in vivo degradability, vascularization and osteogenesis of calcium sulfate-based bone cements containing nanoporous lithium doping magnesium silicate, *Int. J. Nanomed.*, 2017, **12**, 1341–1352.